# Active health monitoring of an aircraft wing with embedded piezoelectric sensor/actuator network: I. Defect detection, localization and growth monitoring

**7 authors**, including:

George Zhao
Intelligent Automation, Inc.
**51** PUBLICATIONS **1,292** CITATIONS

SEE PROFILE

Bulent Ayhan
Signal Processing Inc.
**127** PUBLICATIONS **2,548** CITATIONS

SEE PROFILE

Chiman Kwan
Signal Processing, Inc.
**443** PUBLICATIONS **7,709** CITATIONS

SEE PROFILE

Some of the authors of this publication are also working on these related projects:

Project   Steel Bridge Fatigue Crack Monitoring View project

Project   A High Performance Approach to Local Active Noise Reduction in Noisy Cabins View project

# Active health monitoring of an aircraft wing with embedded piezoelectric sensor/actuator network: I. Defect detection, localization and growth monitoring

**Xiaoliang Zhao**[1,3]**, Huidong Gao**[2]**, Guangfan Zhang**[1]**,
Bulent Ayhan**[1]**, Fei Yan**[2]**, Chiman Kwan**[1] **and Joseph L Rose**[2]

[1] Intelligent Automation Inc., 15400 Calhoun Drive, Suite 400, Rockville,
MD 20855, USA
[2] Department of Engineering Science and Mechanics, The Pennsylvania State University,
University Park, PA 16802, USA

E-mail: xzhao@i-a-i.com

## Abstract

This work focuses on an ultrasonic guided wave structural health monitoring
(SHM) system development for aircraft wing inspection. In part I of the
study, a detailed description of a real aluminum wing specimen and some
preliminary wave propagation tests on the wing panel are presented.
Unfortunately, strong attenuation and scattering impede guided waves for
large-area inspection. Nevertheless, small, low-cost and light-weight
piezoelectric (PZT) discs were bonded to various parts of the aircraft wing, in
a form of relatively sparse arrays, for simulated cracks and corrosion
monitoring. The PZT discs take turns generating and receiving ultrasonic
guided waves. Pair-wise through-transmission waveforms collected at normal
conditions served as baselines, and subsequent signals collected at defected
conditions such as rivet cracks or corrosion detected the presence of a defect
and its location with a novel correlation analysis based technique called
RAPID (reconstruction algorithm for probabilistic inspection of defects). The
effectiveness of the algorithm was tested with several case studies in a
laboratory environment. It showed good performance for defect detection,
size estimation and localization in complex aircraft wing structures.

(Some figures in this article are in colour only in the electronic version)

## 1. Introduction

The flight environment is very harsh due to large changes
in humidity, temperature, pressure, speed, and loading
conditions. These effects cause a lot of stress to the aircraft
frame. As a result, corrosion, delamination, cracks, disbonds,
and other failures creep in once the aircraft is in service for

some time. Traditionally, visual inspection, accompanied by
ultrasound bulk wave or eddy current technology, is often
used to obtain general information on the structural health
conditions. However, the inspection is limited to a point-by-
point manner and is very time consuming. In most cases,
erection of scaffolding or disassembly of the structure is
needed to inspect the interior and inaccessible components,
being very labour intensive and possibly also resulting in

---

[3] Author to whom any correspondence should be addressed.

maintenance-induced damages. The development of a general, *in situ* health monitoring system that can inspect a relatively large area, instantaneously provide reliable and quantitative structural health data such as defect type, location and severity level, minimize and eventually eliminate the need for structural disassembly, and communicate wirelessly and remotely to the inspector or maintenance personnel is the objective and motivation of this study.

Ultrasonic guided waves are elastic waves propagating in solids with boundaries [1–3]. It has been used for non-destructive inspection (NDI) of various defects in aircraft structures [4–6]. Some major advantages of this technique include fast scanning capabilities, low cost, long-range inspection, and testing inaccessible or complex components. Recently, small and conformal piezoelectric ceramics and wafer transducers, either being surface mounted or embedded leave-in-place on the structures, have been widely studied for generating and receiving guided waves for structural integrity monitoring. Keilers and Chang [7], Ihn and Chang [8, 9] and Yang and Chang [10, 11] used the built-in piezoelectric transducers for delamination identification in composite plates, fatigue crack detection and growth monitoring in riveted lap joints and repair patches, and bolt joint loosening inspection in composite thermal protection panels, respectively. A commercial product named SMART layer was developed stemming from the sensor/actuator network concept [12]. Giurgiutiu *et al* [13] studied the ultrasonic waves in beams and plates using an embedded piezoelectric wafer active sensor (PWAS). Maximum coupling is achieved when the PWAS length equals half the wavelength of a particular Lamb wave mode while other modes are minimized. Thus, mode tuning can be achieved with the variation of PWAS dimensions [14]. The composite wing-to-spar bonded joints were inspected with the guided wave PZT disks by Matt *et al* [15]. Several applications of a PZT transducer in various materials and structures such as plates and sandwiched beams were also reported by Lin and Yuan [16], Yang and Qiao [17], and Annamdas and Soh [18]. However, there is still a lack of an effective algorithm to co-operatively process the PZT sensor network data to yield accurate defect detection, size estimation and localization, especially in a large and complex structure where a single and simple defect signal is not readily available due to the effects of multipath, multimodes, strong wave scattering and attenuation, etc.

An aircraft wing is a very complex structure, with all the skin panels, spars, ribs and stiffeners riveted together. Under high cyclic loads or corrosive environment, fatigue cracks may initiate from the rivet holes and go span-wise along the stiffeners or spars. Xiao *et al* [19] reported their study on the fatigue endurance of three aircraft flap-like box structures made of various materials (aluminium alloy, CFRP and GLARE) under acoustic loading. NDT examinations are still needed to characterize those defects. In this paper, the guided wave PZT sensor/actuator network technique was applied to an aircraft wing section for defect monitoring. Specifically, an E-2 surveillance aircraft wing section was cut into pieces for experimental studies. A preliminary test with angle beam Lamb wave transducers on the wing panel was conducted first to evaluate the wave propagation capabilities. Strong attenuations and scattering from the paint and rivet rows
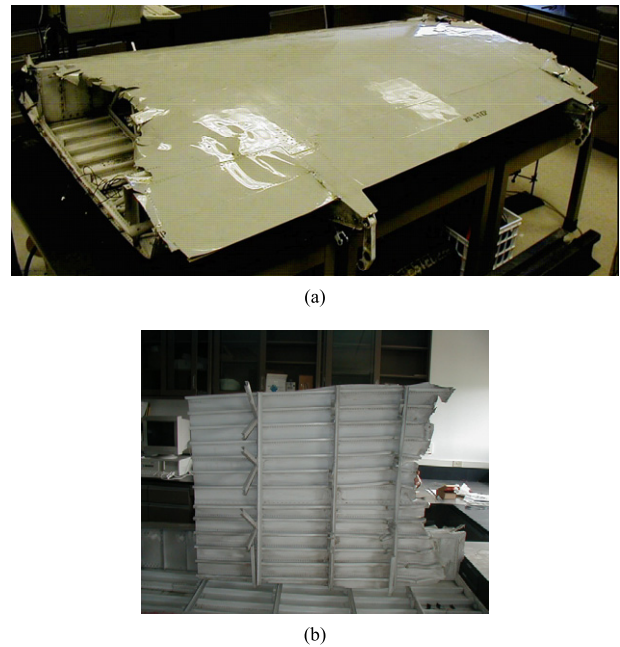


(a)



(b)

**Figure 1.** (a) E-2 surveillance aircraft wing section; (b) the disassembled top panel of the wing.

have a negative influence on the wave inspection range. A relatively sparse PZT array with a diameter of 1 foot was then bonded to the inner surface of the wing to generate and receive ultrasonic guided waves. Simulated defects such as loose rivets, rivet-hole cracks and material loss on the wing panel were studied. To interpret the signals collected from the PZT disc array, a correlation analysis based algorithm called RAPID was developed for defect detection, localization and growth monitoring [20]. Good results were obtained for mapping the simulated defects on the wing panel. It should be noted that the actual defects on an aircraft wing may be different from the machined defects, and the sensor responses are likely to be different. The work presented here intends to demonstrate the feasibilities of the PZT actuator/sensor network and RAPID algorithms for SHM of a real aircraft structure.

## 2. Aircraft wing test-bed description

Figure 1(a) shows an E-2 surveillance airplane wing section that was acquired from the US Navy for this study. It is made of aluminium alloys and coated with paint. For the ease of sensor implementation and experimentation, the top skin of the wing section was disassembled with a plasma cutting tool. Figure 1(b) shows a picture of the disassembled top skin piece. Several samples of the top-skin panel were produced after the dissection, and the inner structures of the wing, such as the D-spars, ribs, and stiffeners, were accessible for the experimental studies.

Figure 2(a) shows a schematic of a piece of the top wing panel and its rivet distribution (in hollow circles). Those rivets are used to fasten the wing panel to the inner structures, such as spars and ribs, but most of them are to strengthen the wing skin with L-shaped stiffeners. Figure 2(b) shows a detailed sketch of a stiffener riveted to the wing skin. As shown in
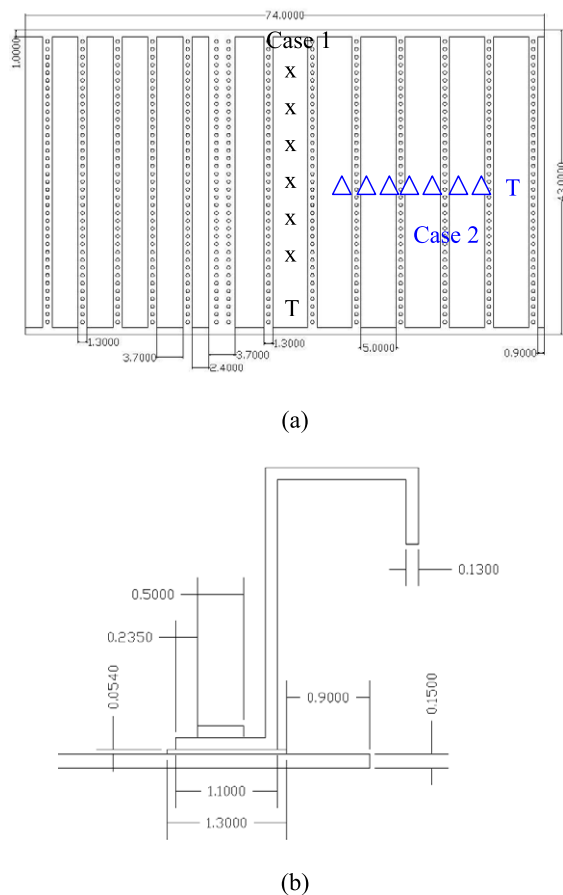
(a)



(b)

**Figure 2.** Wing skin structure: (a) sketch of the rivet row and angle beam transducer locations; (b) typical geometry of a stiffener riveted to the skin (all scales are in centimetres).



**Figure 3.** Guided wave signals between rivet rows show the wave attenuation with propagation distance.

figure 2(b), the wing skin is a bit thicker under the stiffeners than where there is no stiffener. Thickness measurement was carried out with a micrometer. The average thicknesses of the wing skin with paint are about 1.08 and 1.51 mm, respectively, at different wing sections, and the additional thickness beneath the stiffener varies from 0.3 to 0.6 mm.

The geometric complexities of the wing panel lead to complicated ultrasonic guided wave propagation characteristics. The conventional uniform-thickness plate model is not directly applicable here, since the thickness variation leads to variations in wave speed, mode shape, and mode conversion etc. The wing skin is also coated with at least two layers of paint on the outer surface and one on the inner surface, which attenuates the ultrasonic energy substantially. In addition, the wing panel is distributed with rivet rows in every 6.5 cm and the rivets are spaced less than 9 mm from each other. This introduces great energy scattering and blockage for waves across the rivet rows. We performed an initial wave propagation study on the wing panel with two angle beam transducers in a through-transmission mode. In the first case, the transducers were put in between two adjacent rivet rows and the receiver moved away from the transmitter ($T$), following the 'x' line in figure 2(a). Thus the wave propagates mostly parallel to the rivet rows. Figure 3 shows the sample 1.8 MHz $S_0$ mode Lamb wave signals collected when the receiver transducer was 20–200 mm away
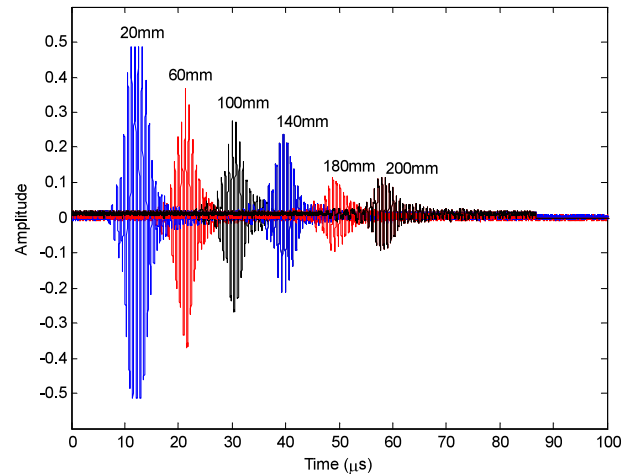
from the transmitter. Wave amplitude reduction is quite noticeable with distance due to beam spreading, wave leakage to the paint, and attenuation. The average signal attenuation rate was around 0.044 dB mm$^{-1}$ for the $S_0$ mode Lamb wave. In the second case, the transducers were put perpendicular to the rivet rows, with the receiver locations shown in figure 2(a) as '$\Delta$'s. The 1.8 MHz $S_0$ mode Lamb wave propagated across the rivet rows and an average amplitude attenuation of 15 dB was observed for passing each row, of which about 9 dB was caused by rivet scattering, plate thickness variation, wave leakage to the stiffener bond joint, etc. The signal shape was also no longer a pure single burst like those in figure 3 but rather extended in the time domain with multi-path/scattering signals coming in (not shown here). From the above study, it was observed that the attenuation, wave leakage and scattering effects certainly restricted the inspection range of the guided waves. A practical effective range should be estimated or measured before implementing the guided wave actuator/sensor networks.

## 3. PZT transducer array network for wing panel SHM

Lead zirconate titanate (PZT) is a piezoelectric material with a high electromechanical coupling coefficient. It is widely used in acoustic and ultrasonic devices to generate and receive acoustic waves. The PZT disc transducers used in our experiment are made of PZT ceramics with silver electrodes on both sides of the discs. They were ordered from American Piezo Ceramics Inc (material model 850). When the transducer is electrically polarized in the thickness direction, several vibration modes can be excited by applying an ac voltage between the top and bottom electrode. A sample of the PZT disc transducer used in our experiment is shown in figure 4. The thickness and diameter of the ceramic are 10 mils (0.254 mm) and 1/4 in. (6.3 mm), respectively. Generally, two vibration modes can be excited in this thickness polarized disc: thickness mode and radial mode. The mode frequencies are controlled by the design parameters of the thickness and diameter together with the material properties. Radial resonance was used in this ultrasonic guided wave experiment.
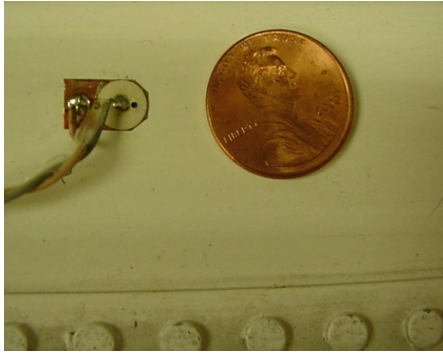
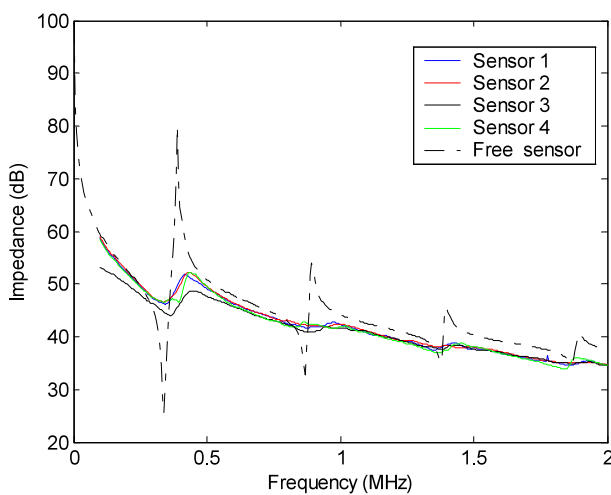**Figure 4.** The overall size of the surface mounted PZT sensor/actuator.



**Figure 5.** The impedance spectra of a free PZT disc and sample PZT discs when mounted on the wing panel.



**Figure 6.** PZT sensor/actuator array attached at the inner surface of the wing panel for defect monitoring.

Thickness resonance can also be observed with comparably lower wave excitation efficiency at higher frequency.

To attach a PZT sensor to the wing structures, the surface of the wing section is cleaned first with alcohol, and a copper tape is attached to the cleaned surface. Then a PZT disc is glued on top of the copper tape with conductive epoxy. Finally, a lead wire is soldered or glued with conductive epoxy to the top surface of the sensor to serve as the signal wire and the copper tape is used as the electrical ground. To insulate the sensor and protect it from shock or vibration, the sensor assembly could be covered with epoxy, with only the signal and ground wires leading out. The electric mechanical impedances of the sensors were measured with an impedance analyser (HP 4192) to check their performance. The decibel scale impedance was obtained from the reading of an impedance analyser's $Z_\Omega$ with $Z_{dB} = 20 \log_{10}(|Z_\Omega|)$. In figure 5, the dashed curve shows the free vibration disc in air; and the solid curves show the PZT impedance after being bonded to the wing panel. The resonance frequency around 350 kHz shown in the free vibration curve corresponds to the resonance in the radial direction of the disc. The higher-order resonances are the corresponding harmonics. When the sensor is attached to the wing skin, the resonance phenomenon is not as significant as the free vibration condition. However, operation around
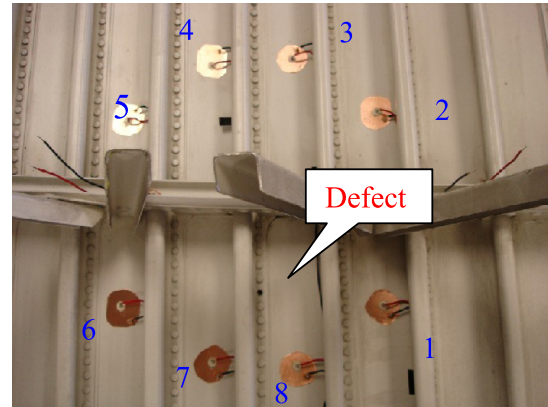
350 kHz still has good wave excitation efficiency. Furthermore, the sensor implementation uniformity and potential differences in the mechanical properties of the wing panel cause slight differences in the impedance spectra of these attached sensors.

For demonstration purposes, a circular array configuration of the PZT transducer network was implemented on the wing panel for defect monitoring. Such a configuration should be useful for monitoring a well-defined region or a structural 'hot spot' where defects are most likely to occur. In our study, eight piezo-ceramic discs were attached to the aircraft wing surface in a circle about 10 inches in diameter. The discs are nearly equally spaced. Figure 6 shows the example array, with arabic numbers $1, 2, \ldots, 8$ marked nearby to identify each PZT. A MATEC TB-1000 tone burst pulser/receiver card was used to generate and receive the ultrasonic signals. A 100 V peak-to-peak 350 kHz windowed sinusoidal signal (three to four cycles) was used to drive the PZT actuator. The PZT discs take turns generating ultrasonic signals while the rest of them are listening. For example, when disc 1 is sending a signal, sensors 2–8 are in the reception mode; then disc 2 is transmitting signals and sensors 1, 3–8 are listening, and so on. The waveforms of each actuator-sensor pairs are collected. Figure 7 shows an example waveform collected from actuator-sensor pairs 1 and 8 with and without a crack. Note that at 350 kHz, $S_0$ and $A_0$ mode Lamb waves could exist in the wing panel; besides, the scattering of the guided waves from the rivet rows also complicated the waveform, therefore it is difficult, if not impossible, to identify the wave modes from the raw signal. A physics-based statistical data processing algorithm is thus developed for real-time processing of the data so that the defect presence, growth, and location can be monitored effectively. Of course, for applying the PZT actuator/sensor network to a general structure, the single circular array configuration could be expanded to a network of arrays in hexagons, for example, so that a large structural area could be monitored.

## 4. Defect characterization with correlation analysis and RAPID

Defect detection, growth monitoring and location mapping with guided wave arrays has been studied through computer tomography approaches, using wave speed, attenuation or
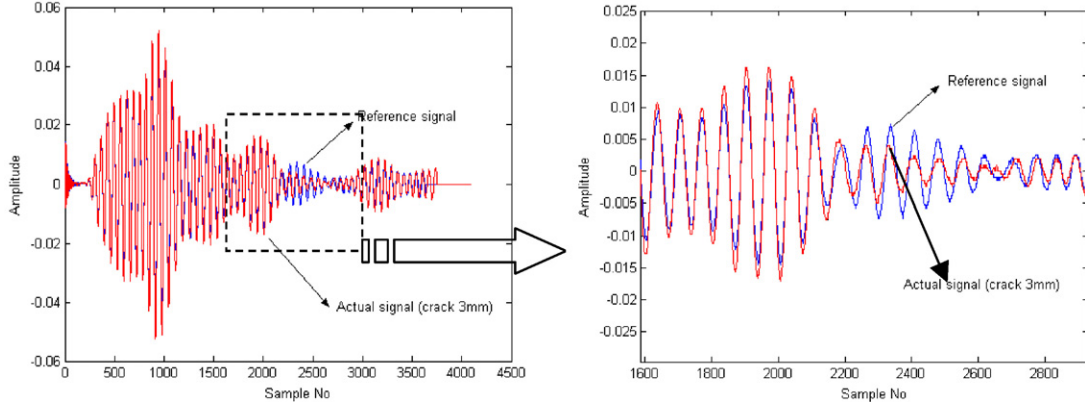
**Figure 7.** Sample waveforms of the sensor pair (1, 8). One curve is for reference (normal condition) and the other is from the rivet hole with a 3 mm crack. The figure on the right is the zoom-in of the dashed window.

energy as features for image reconstruction [21, 22]. While accurate defect images can be obtained, however, those approaches are quite time consuming and the sensitivity is not satisfactory with sparse sensors. A simple yet effective correlation analysis technique was developed in this study to detect small defects by measuring the differences in the guided wave signals between normal and faulty conditions. Specifically, the initial waveforms taken after the sensor array is installed on a structure are used as the reference data. New signals collected afterwards are compared with the reference data to identify if there is a major change in the signal characteristics. Given the same environmental and measurement conditions, this change is attributed to the defect initiation. The growth of the defect can also be monitored by tracing the increase in the signal difference from the normal condition. In a simple mathematical formula, the signal change can be represented by a correlation coefficient $\rho$ given by

$$\rho = \frac{C_{XY}}{\sigma_X \sigma_Y} \qquad (1)$$

where $C_{XY}$ is the covariance of $X$ and $Y$ given by

$$C_{XY} = \sum_{k=1}^{K} (X_k - \mu_x)(Y_k - \mu_y) \qquad (2)$$

where $\mu$ is the mean of the respective data set and $K$ is the length of the data set. In this case, the data set $X$ is the reference data and $Y$ is each new set of data recorded after a period of service time. $\sigma_x$ and $\sigma_y$ are the standard deviations of $x$ and $y$, respectively, with their product given by

$$\sigma_X \sigma_Y = \sqrt{\sum_{k=1}^{K} (X_k - \mu_X)^2} \sqrt{\sum_{i=1}^{K} (Y_k - \mu_Y)^2}. \qquad (3)$$

In order to determine the location of the defect, we assume that the probability of a defect occurrence at a certain point can be estimated from the severity of the signal changes of different sensor pairs as a result of this defect and its relative position to the sensor pairs. The physical intuition behind this is that a defect would cause the most significant signal change in the direct wave path, and that the signal change effect would
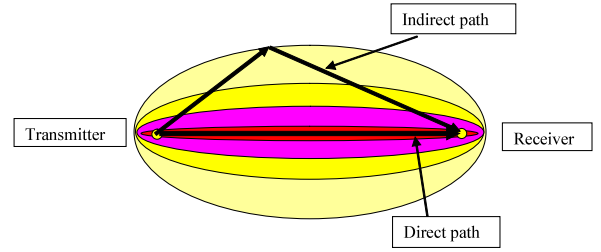


**Figure 8.** Illustration of the elliptical distribution function of the RAPID algorithm.

decrease if the defect is away from the direct path of the sensor pair. (Note that there might be cases that mirror reflection exists with the defect and the above assumption does not apply; the statistical nature of multiple sensor pairs can accommodate it to some extent.) The defect distribution probability within the sensor network can thus be expressed as a linear summation of all the signal change effects of every possible transmitter-receiver pair, each of which has a spatial distribution. Here a simple linearly decreasing elliptical distribution is assumed, with the transmitter and receiver PZT at the foci. Assuming there are total $N$ PZT elements in an array cluster of a sensor network, the estimation of the defect probability at position $(x, y)$ within the reconstruction region $P(x, y)$ can be written as

$$P(x, y) = \sum_{i=1}^{N-1} \sum_{j=i+1}^{N} P_{ij}(x, y)$$
$$= \sum_{i=1}^{N-1} \sum_{j=i+1}^{N} A_{ij} \left[ \frac{\beta - R_{ij}(x, y)}{\beta - 1} \right]. \qquad (4)$$

Here, $P_{ij}(x, y)$ is the defect distribution probability estimation from the transmitter $i$ and receiver $j$ sensor pair, $S_{ij}$. $A_{ij}$ is the signal difference coefficient (SDC) of the sensor pair $S_{ij}$ and $A_{ij} = 1 - \rho_{ij}$, following equation (1). Note that, due to reciprocity, the signal collected from sensor pair $S_{ji}$ should be the same as that from $S_{ij}$, thus only $N(N-1)/2$ sets of data are needed. In the real experiment, the signal of sensor pair $S_{ji}$ was still collected for verification and averaging purpose. $(\beta - R_{ij}(x, y))/(\beta - 1)$ is the non-negative linearly decreasing

(a)
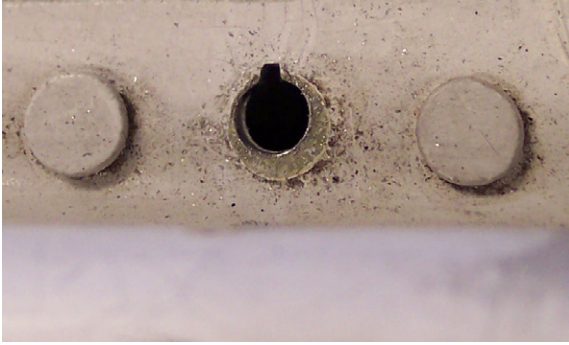


(b)



(c)

**Figure 9.** Photos of an artificial saw-cut defect introduced in a rivet hole: (a) rivet drilled off; (b) 1 mm crack; (c) 3 mm crack.

spatial distribution function of $S_{ij}$, with its contour in the shape of a set of ellipses. Figure 8 shows the geometric interpretation of this distribution function. In the formula,

$$R_{ij}(x, y) = \begin{cases} RD_{ij}(x, y) & \text{when } RD_{ij}(x, y) < \beta \\ \beta & \text{when } RD_{ij}(x, y) \geqslant \beta, \end{cases} \quad (5)$$
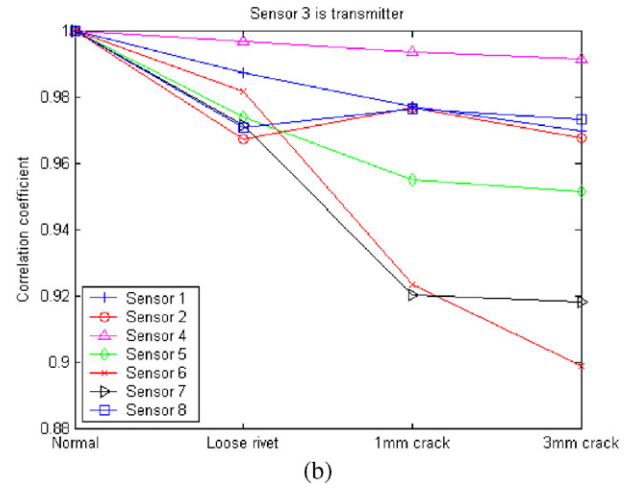
where

$$RD_{ij}(x, y)$$
$$= \frac{\sqrt{(x - x_i)^2 + (y - y_i)^2} + \sqrt{(x - x_j)^2 + (y - y_j)^2}}{\sqrt{(x_j - x_i)^2 + (y_j - y_i)^2}} \quad (6)$$

is the ratio of the sum of distance of the point $(x, y)$ to the transmitter $i$ and receiver $j$ (the focal radii) to the distance between the transmitter and receiver. $\beta$ is a scaling parameter
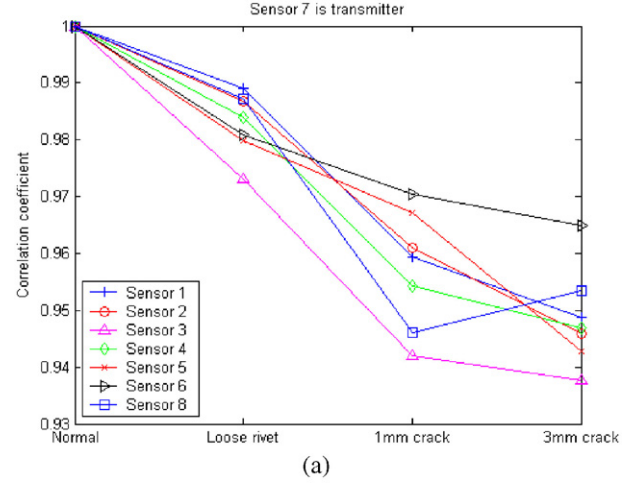


(a)



(b)

**Figure 10.** Correlation coefficients of the collected signals with reference signals for defect detection and growth monitoring: (a) sensor 7 is the transmitter, and all the others are receivers; (b) sensor 3 is the transmitter, and all the others are receivers.

which controls the size of the effective elliptical distribution area, and $\beta > 1$. When $R_{ij}(x, y) = 1$, i.e. the point $(x, y)$ is on the direct line of the transmitter–receiver pair $S_{ij}$, $P_{ij}(x, y) = A_{ij}(x, y)$; when $R_{ij}(x, y) = \beta$, i.e. the point $(x, y)$ is on the boundary of the effective distribution area, $P_{ij}(x, y) = 0$. Usually, $\beta$ is selected to be around 1.05. Artifacts will be introduced if $\beta$ is too small, and resolution is lost if $\beta$ is too large. Generally, if a defect occurs, a set of sensor pair signals will be affected. As a result, in the defect distribution probability image, the point where the defect is located will have dominantly larger probability compared to the other points. Consequently, by applying image processing techniques, such as judiciously selecting a threshold to the defect estimation image, the defect location can be estimated.

## 5. Experimental studies on the wing specimens

### 5.1. Rivet crack monitoring on the wing panel

In this experiment, the wing panel shown in figure 6 was used as a specimen to monitor cracks that were initiated from the
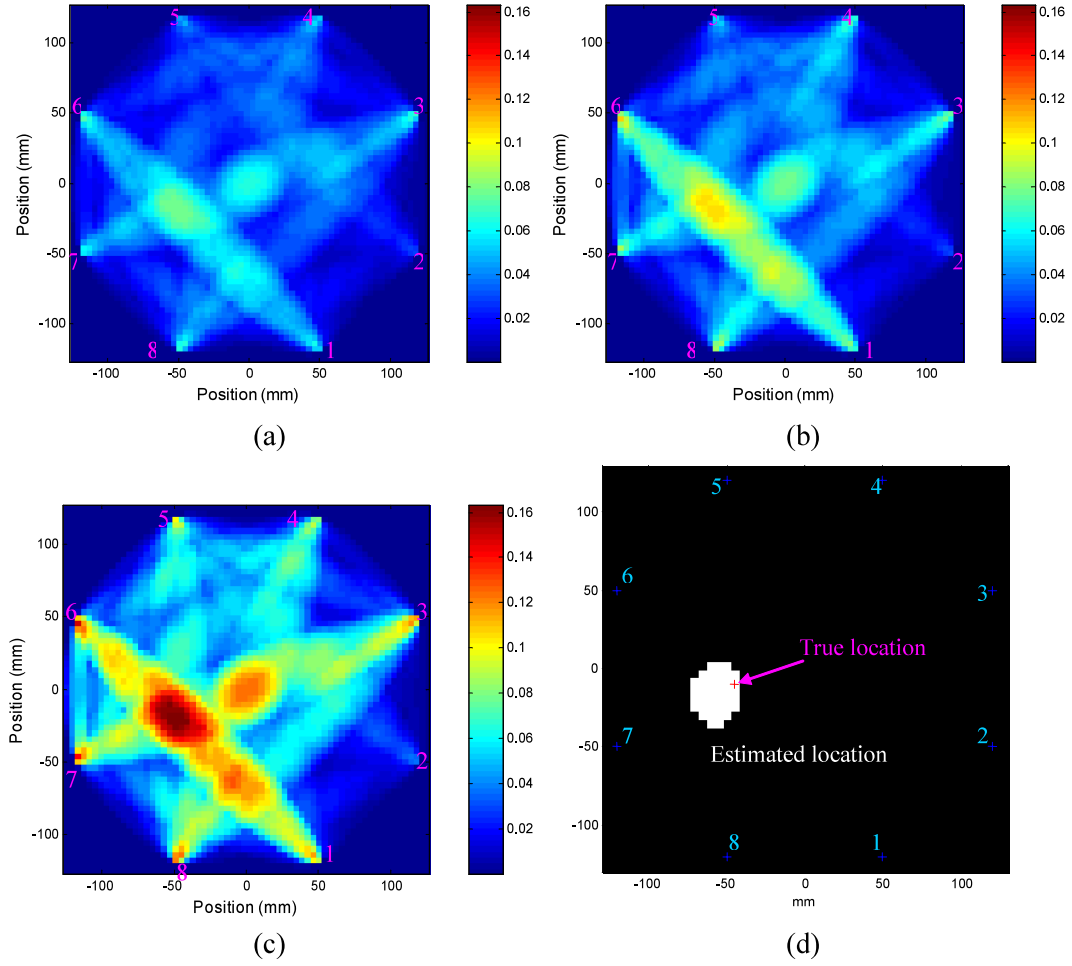
**Figure 11.** Defect location estimation with RAPID. The defect distribution probability map shows the location of the defect and its progression: (a) loose rivet; (b) 1 mm crack in the rivet hole; (c) 3 mm crack in the rivet hole; (d) the estimated defect location by setting a threshold to the probability density map.

rivet holes. Four conditions were studied, i.e. (a) the normal, defect-free condition; (b) a rivet was driven out of the wing panel and then put back in to simulate a loose rivet; (c) a 1 mm notch was machined in the loose-rivet hole to simulate a small crack; and (d) the rivet crack was increased to 3 mm. Figure 9 shows the three defect pictures. As mentioned in section 3, a MATEC tone-burst pulser/receiver card was used to generate and collect pair-wise PZT sensor signals. The baseline ultrasonic guided wave data for the normal condition were collected first, and the data for each defect condition were collected afterwards.

The correlation analysis and RAPID algorithm described in section 4 was used to detect the defect, track its growth, and localize its position. The correlation coefficients of different stages of the defects, namely a normal, loose-rivet, 1 mm-crack, and 3 mm-crack are calculated for different pairs of sensors. Figure 10(a) shows the sample correlation coefficient plots versus failure stages when sensor 7 was used as the transmitter while the others were receivers. The correlation coefficient values for all the receivers are plotted using different symbols. Since the defect location is very close to sensor 7, all the receivers picked up the defect signature.

The correlation coefficients decreased in value with an increase in the defect severity level. So the defect growth could be monitored with careful calibration. Of course, not all of the sensor pairs showed the same amount of decrease in correlation coefficient value with respect to the crack growth. In this case, sensor 3 shows the largest decrease in the correlation coefficient, since the defect is in the direct path of sensors 7 and 3. Similarly, Figure 10(b) shows the correlation coefficients' change plots with respect to defect growth when sensor 3 was used as the transmitter. We can see that sensors 6 and 7 have the largest decrease in correlation coefficient value while sensor 4 shows almost no change. This also indicates that correlation analysis cannot only monitor the defect growth but also be used to estimate the defect location.

The RAPID algorithm developed in section 4 was then used to determine the defect location. The probabilistic distribution maps for each stage of the defect, i.e. loose-rivet, 1 mm rivet crack, and 3 mm rivet crack, were reconstructed on the basis of equations (4)–(6) and plotted in MATLAB®, as shown in figures 11(a)–(c). In each image, the higher the probability density value is, the higher the chance that the defect is located there. We could also see that the overall
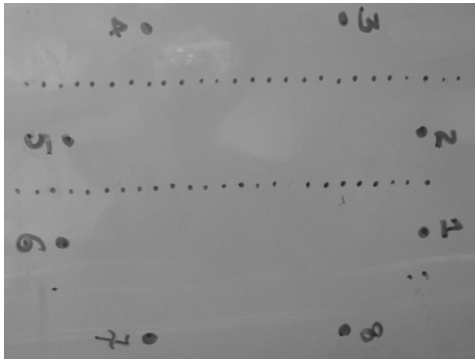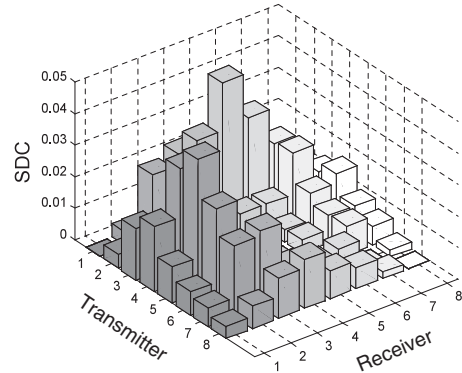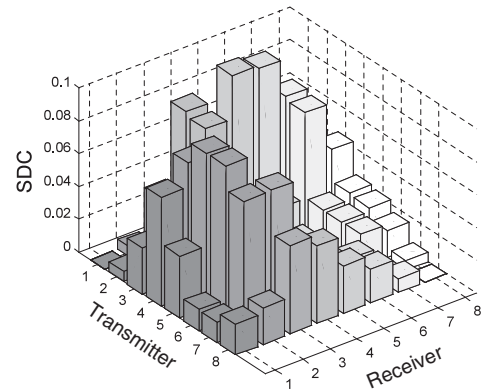
(a) Reference state
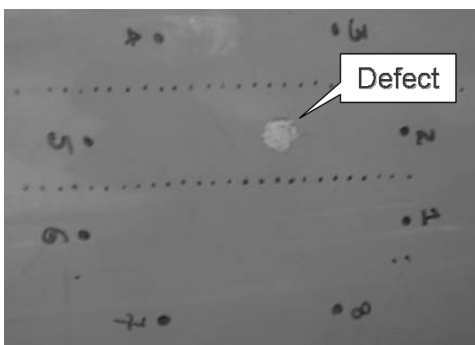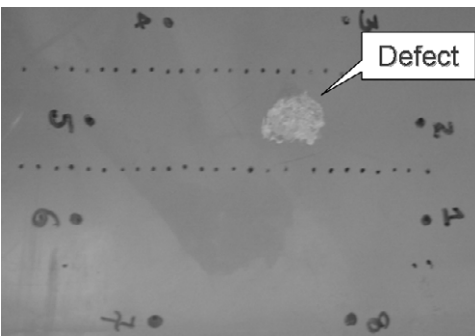


(b) Small corrosion



(c) Larger corrosion

**Figure 12.** Simulated corrosion defects: (a) reference state; (b) small corrosion; (c) large corrosion.



(a) Small corrosion area



(b) Large corrosion area

**Figure 13.** Signal difference coefficients for small and large simulated corrosion on the wing panel.

probability value increases with an increase in the defect severity level, as indicated from the image colour progression in figures 11(a)–(c). With a proper threshold value set to the defect probability density map regarding the defect, the estimated defect location, which is shown in figure 11(d), is found to agree quite well with the actual defect location. It can be seen that the RAPID algorithm works effectively with the PZT actuator/sensor network for small defect detection and localization. It also showed better sensitivity compared with conventional filtered back-projection computer tomography in another study [23].

### 5.2. Simulated corrosion monitoring

As another case study, simulated corrosion defects were introduced by grinding the paint and some metal off at the outer wing skin. Three stages of corrosion on the wing were studied: the reference normal state, a small simulated corrosion area, and a large corrosion area. Pictures taken from the top surface of the wing of these three states are shown in figure 12. The corresponding sensor positions at the inner surface are also marked on the outer surface of the wing skin. The signal difference coefficients (SDC) of these corrosion states are shown in figure 13, where the $x$ and $y$ axes denote the transmitter and receiver PZTs and the $z$ axis is the SDC of the combination transmitter–receiver pair. The progression of structural damage is indicated with a general increase of the SDC feature. In addition, the geometric distribution of the damage is also indicated with the difference in SDCs for different sensor pairs. With the RAPID algorithm, the corrosions were mapped as the dark red area, as shown in figure 14. A circle is marked on the map as the true size and location. An accurate estimation of the corrosion location can be seen when compared with the true location. The size of the corrosion could also be estimated, though not exactly, with proper calibration.
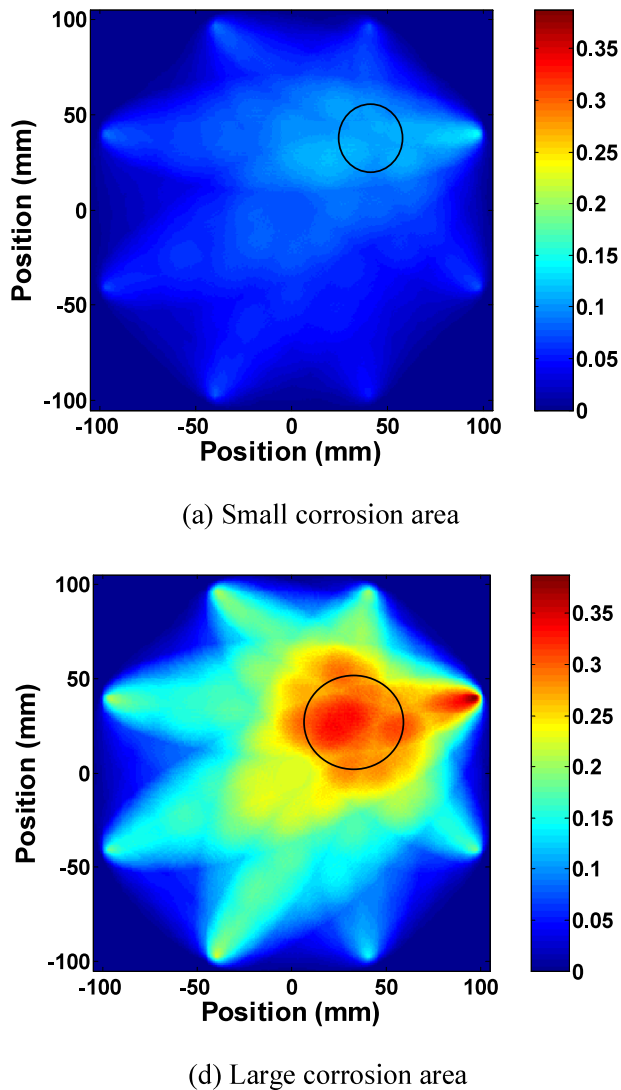
(a) Small corrosion area



(d) Large corrosion area

**Figure 14.** Reconstruction image of the corrosion damage distribution.

## 6. Conclusions

In this paper, a piezoelectric-based embedded sensor/actuator network was applied to an aircraft wing for structural integrity monitoring. A preliminary survey on the wing panel with angle beam guided wave transducers revealed the difficulties of wave propagation over a long distance in the panel due to strong attenuation from paint and rivet scattering. Nevertheless, a circular sparse array of eight-element PZT discs was implemented on the inner surface of the wing about a foot in diameter to monitor any cracks or corrosion on the wing, and waveforms from all combinations of the transmitter–receiver pairs were collected. A correlation analysis based probabilistic defect detection and localization algorithm was developed to process the senor network data, and the signal difference coefficients of the sensor pairs were used to reconstruct the defect distribution probability map to estimate the location of the defect and to monitor its growth. The effectiveness of the algorithm was thoroughly tested over several simulated defect types and stages and showed great potential for on-line interpretation of networked PZT sensor data for structural health monitoring of an aircraft wing. More tests on real defects may be needed to further prove the effectiveness of this approach.

## References

[1] Lamb H 1917 On waves in an elastic plate *Proc. R. Soc.* A **93** 114–20
[2] Viktorov I A 1970 *Rayleigh and Lamb Waves* (New York: Plenum)
[3] Rose J L 1999 *Ultrasonic Waves in Solid Media* (Cambridge: Cambridge University Press)
[4] Mal A and Chang Z 1998 NDE of rivet holes in aging aircraft components using lamb waves *Proc. SPIE* **3397** 68–75
[5] Rose J L and Soley L 2000 Ultrasonic guided waves for the detection of anomalies in aircraft components *Mater. Eval.* **50** 1080–6
[6] di Scalea F L *et al* 2002 Guided wave ultrasonics for NDE of aging aircraft components *Proc. SPIE* **4704** 123–32
[7] Keilers C H and Chang F K 1995 Identifying delamination in composite beams using built-in piezoelectrics *J. Intell. Mater. Syst. Struct.* **6** 649–72
[8] Ihn J B and Chang F K 2004 Detction and monitoring of hidden fatigue crack growth using a built-in piezoelectric sensor/actuator network: I. Diagnostics *Smart Mater. Struct.* **13** 609–20
[9] Ihn J B and Chang F K 2004 Detction and monitoring of hidden fatigue crack growth using a built-in piezoelectric sensor/actuator network: II. Validation using tiveted joints and repair patches *Smart Mater. Struct.* **13** 621–30
[10] Yang J and Chang F K 2006 Detection of bolt loosening in C–C composite thermal protection panels: I. Diagnostic principle *Smart Mater. Struct.* **15** 581–90
[11] Yang J and Chang F K 2006 Detection of bolt loosening in C–C composite thermal protection panels: II. Experimental verification *Smart Mater. Struct.* **15** 591–9
[12] Lin M, Qing X, Kumar A and Beard S 2001 SMART layers and SMART suitcase for structural health monitoring applications *Proc. SPIE* **4332** 98–106
[13] Giurgiutiu V, Bao J and Zhao W 2003 Piezoelectric wafer active sensor embedded ultrasonics in beams and plates *Exp. Mech.* **43** 428–49
[14] Giurgiutiu V 2005 Tuned Lamb wave excitation and detection with piezoelectric wafer active sensors for structural health monitoring *J. Intell. Mater. Syst. Struct.* **16** 291–305
[15] Matt H, Bartoli I and di Scalea F L 2005 Ultrasonic guided wave monitoring of composite wing skin-to-spar bonded joints in aerospace structures *J. Acoust. Soc. Am.* **118** 2240–52
[16] Lin X and Yuan F G 2001 Dianostic Lamb waves in an integrated piezoelectric sensor/actuator plate: analytical and experimental studies *Smart Mater. Struct.* **10** 907–13
[17] Yang M and Qiao P 2005 Modeling and experimental detection of damage in various materials using the pulse-echo method and piezoelectric sensor/actuators *Smart Mater. Struct.* **14** 1083–100
[18] Annamdas V and Soh C K 2006 Embedded piezoelectric ceramic transducers in sandwiched beams *Smart Mater. Struct.* **15** 538–49

[19] Xiao Y, White R G and Aglietti G S 2005 Comparison of structural response and fatigue endurance of sircraft flap-like box structures subjected to acoustic loading *J. Acoust. Soc. Am.* **117** 2820–34

[20] Gao H, Shi Y and Rose J L 2005 Guided wave tomography on an aircraft wing with leave in place sensors *Rev. Prog. QNDE, AIP Proc.* **760** 1788–94

[21] Malyarenko E V and Hinders M K 2001 Lamb wave diffraction tomography *Ultrasonics* **39** 269–81

[22] Prasad S M, Balasubramaniam K and Krishnamurthy C V 2004 Structural health monitoring of composite structures using Lamb wave tomography *Smart Mater. Struct.* **13** N73–9

[23] Hay T R *et al* 2006 A comparison of embedded sensor Lamb wave ultrasonic tomography approaches for material loss detection *Smart Mater. Struct.* **15** 946–51